PEROVSKITES

Molecularly thin, two-dimensional all-organic perovskites

Hwa Seob Choi[1]†, Jun Lin[1]†, Gang Wang[2]†, Walter P. D. Wong[3], In-Hyeok Park[4], Fang Lin[5], Jun Yin[1]*, Kai Leng[1,6]*, Junhao Lin[2,7]*, Kian Ping Loh[1]*

Recently, the emergence of all-organic perovskites with three-dimensional (3D) structures has expanded the potential applications of perovskite materials. However, the synthesis and utilization of all-organic perovskites in 2D form remain largely unexplored because the design principle has not been developed. We present the successful synthesis of a metal-free 2D layered perovskite, denoted as the Choi-Loh van der Waals phase (CL-v phase), with the chemical formula $A_2B_2X_4$, where A represents a larger-sized cation compared to B and X denotes an anion. The CL-v phase exhibits a van der Waals gap enabled by interlayer hydrogen bonding and can be exfoliated or grown as molecularly thin 2D organic crystals. The dielectric constants of the CL-v phase range from 4.8 to 5.5 and we demonstrate their potential as gate dielectrics for thin-film transistors.

Perovskite materials are not only of fundamental interest but also display properties that enable applications including ferroelectrics (*1*), quantum materials (*2*), catalysts (*3*, *4*), light-emitting devices (*5*), and solar cells (*6*). Perovskite crystals have a stoichiometry of ABX_3, where A represents a larger cation compared with B, X denotes an anion, and B is coordinated to six X anions to form a BX_6 octahedron. In three-dimensional (3D) perovskites, these octahedra share corners and the A cation occupies the cuboctahedral site surrounded by eight octahedra. By disrupting the continuous linkage of the octahedra along the [001]direction, a 2D version of perovskites can be formed in which layered structures are separated by van der Waals gaps.

Depending on the interlayer offset and the type of atoms present in the "spacer" layer, 2D perovskites can be classified into the Ruddlesden-Popper phase (RP phase) (*7*, *8*), the Dion-Jacobson phase (DJ phase) (*9*), and the Aurivillius phase (*10*, *11*). The RP and DJ phase layered perovskites have general formulas of A_2BX_4 and ABX_4, respectively. These structures typically consist of corner-shared BX_4 octahedra forming a 2D layer, with the A^+ cations coordinated to the cuboctahedral sites above and below the BX_4 octahedra layer to maintain overall charge neutrality.

The synthesis of all-organic perovskites has been recognized as a challenging task within the scientific community (*12*–*29*). In principle, the structural topology of perovskite can be maintained by replacing A, B, and X ions with appropriately sized organic molecules, as dictated by the Goldschmidt tolerance factor for relative ion sizes. However, in practice, only a few organic molecules (among those currently used) fulfill this criterion. The isostructural family of dicationic piperazinium organic perovskites with Cl^-, Br^-, and I^- was discovered as recently as 2002 (*12*). More recently, Xiong *et al.* synthesized a diverse class of organic perovskites by designing various diammonium cations, resulting in the report of 23 different organic 3D perovskites (*14*). These compounds include a few ferroelectrics such as MDABCO-NH_4-I_3 (MDABCO = *N*-methyl-1,4-diazabicyclo[2.2.2] octonium), which have polarization properties (22 μC/cm^2) similar to those of $BaTiO_3$.

Aside from 3D metal-free perovskites, we ask whether 2D-version (layered packing), metal-free perovskites can be synthesized. The presence of a van der Waals gap in 2D perovskites offers the advantage of incorporating larger organic cations through self-adjustable strain-balancing within the layered structures, which could overcome steric effects that hinder 3D perovskite synthesis (*30*). This expanded library of larger and more exotic A-site cations in 2D perovskites could enable the emergence of distinctive properties and applications. We present the design principles and synthesis of a new class of all-organic layered 2D perovskite phases. Following the naming convention of oxide perovskites, we refer to these as Choi-Loh van der Waals phase (CL-v phase), with the suffix v denoting van der Waals stacking in the structure. The CL-v phase layered perovskites can be exfoliated or grown as ultrathin layers of several nanometers.

[1]Department of Applied Physics, Hong Kong Polytechnic University, Hung Hom, Kowloon, Hong Kong, China. [2]Department of Physics, Southern University of Science and Technology, Shenzhen 518055, China. [3]Department of Chemistry, National University of Singapore, Singapore 117543, Singapore. [4]Graduate School of Analytical Science and Technology (GRAST), Chungnam National University, Daejeon 34134, Republic of Korea. [5]College of Electronic Engineering, South China Agricultural University, Guangzhou 510642, China. [6]The Hong Kong Polytechnic University Shenzhen Research Institute, Shenzhen 518057, China. [7]Quantum Science Center of Guangdong–Hong Kong–Macao Greater Bay Area (Guangdong), Shenzhen 518045, China.
***Corresponding author. Email: jun.yin@polyu.edu.hk (J.Y.); linjh@sustech.edu.cn (J.L.); kathy-kai.leng@polyu.edu.hk (K.L.); kian-ping.loh@polyu.edu.hk (K.P.L.)**
†These authors contributed equally to this work.

Design strategy for 2D all-organic perovski

Charge-balance considerations prohibit the existence of an RP-type all-organic perovskite with the stoichiometry of A_2BX_4 (Fig. 1A). The smallest B-site cation in all-organic perovskites is the monovalent ammonium cation (NH_4^+), whereas B-site cations in hybrid organic-inorganic perovskites (HOIPs) are typically divalent metal ions such as Pb^{2+} and Sn^{2+}. Thus, the BX_4 octahedral layers (X indicates a halogen) in all-organic perovskites possess a −3 charge, in contrast to the −2 charge found in HOIPs (Fig. 1B). To maintain charge neutrality, an odd-numbered counter charge is required, with the geometric constraint that A-site cations must exclusively occupy the cuboctahedral sites. We proposed that this charge balance could be achieved if an additional NH_4^+ cation per unit cell occupied an "interstitial" position between the layers and transform A_2^{2+} into A_2B^{3+} (Fig. 1C). The combination of the BX_4^{3-} and A_2B^{3+} layers results in the stoichiometry $A_2B_2X_4$, abbreviated as ABX_2. The critical challenge in this design approach lies in ensuring the stability of the additional B^+ cation at the interstitial position, which depends on its surrounding bonding environment.

In a typical cubic unit cell there are four sites available for occupation: the corner, body center, face center, and edge center sites (Fig. 2A). In the case of a perovskite unit cell, anions occupy the face center site (X-site), the small cation occupies the body center site (B-site) to form an octahedron with the anions, whereas the large cation occupies the corner site (A-site) to form a cuboctahedron with the anions. The interstitial site at the edge center (E-site) can be filled by the small B^+ cation (Fig. 2B). Our design for the all-organic lattice used *N*-chloromethyl-1,4-diazabicyclo[2.2.2]octonium (CMD^+) as the A-site cation because it could form hydrogen bonds both laterally and orthogonally with the interstitial B^+ cation at the edge center (E-site) of the unit cell (fig. S1). The B-site was occupied by NH_4^+ and the X-site was occupied by PF_6^-. In the case of CMD^+, the lone pair at the nitrogen formed an N-H···N hydrogen bond with NH_4^+-edge laterally, whereas the chloromethane from the adjacent layer formed an N-H···Cl hydrogen bond with NH_4-edge vertically, thus stabilizing it by forming an NH_4^+-edge$[PF_6]_3[N]_2[Cl]$ octahedron (Fig. 2C).

Structure description of CL-v phases

We synthesized CMD-N-P_2 through the slow diffusion of dichloroethane into an acetone solution containing CMD-PF_6 and NH_4PF_6. A hexagonal-shaped single crystal of CMD-N-P_2 measuring 9 × 7 × 0.5 mm was obtained (Fig. 2E, inset). The crystal structure was monoclinic and belonged to the $P2_1/n$ symmetry group, as determined by single-crystal x-ray diffraction analysis (see supplementary materials, table S1).

To present the crystal structure, we chose a unit cell similar to the conventional perovskite structure. Using a transformation matrix (see supplementary materials), we transformed the unit cell into a 4×4×4 supercell composed of 64 pseudo-cubic unit cells (fig. S2). We defined the [001] direction as normal to the octahedral layers.

The pseudo-cubic unit cell consisted of one NH_4^+ cation occupying the body center site and four PF_6^- anions occupying the X-site to form a homo-octahedron with NH_4^+-body, creating the basal BX_4 corner-shared octahedral layer (Fig. 2B octahedra, NH_4^+-body[PF_6]$_6$). Another NH_4^+ cation occupied the edge center at the bottom and top surfaces of the (001) plane of the pseudo-cubic unit cell, which was shared with an adjacent unit cell (Fig. 2B and fig. S3). The occupancy at the edge center was ½ as a result of sharing between two pseudo-cubic unit cells in the layered structure (fig. S4). Only one of the four edges of either the top or bottom surface was occupied by NH_4^+-edge, resulting in a total occupancy of 1 in the pseudo-cubic unit cell for charge balancing. CMD^+ occupied the eight-cornered A-site cation positions (Fig. 2B). The neutral nitrogen atoms from the heads of the two CMD^+ ions coordinated with NH_4^+-edge (Fig. 2, B and C, blue dotted line), and the three PF_6^- ions stabilized NH_4^+-edge in a square pyramidal site (Fig. 2C, translucent red pyramid).

In the next layer the Cl atom at the tail of the CMD^+ ion stabilized the structure through an N-H···Cl interaction, with a Cl–N distance of 4.204(1) Å. Thus, a hetero-octahedron (where coordinating atoms or molecules are different) formed with three PF_6^-, two N from CMD^+, and one Cl from CMD^+ in the adjacent layer (Fig. 2C, NH_4-edge[PF_6]$_3$[N]$_2$[Cl]). The interlayer interaction was predominantly governed by hydrogen bonding between NH_4^+-edge and the Cl atom of the CMD^+ ion across the two layers (Fig. C and F). Only half of the Cl from the CMD^+ ion was hydrogen bonded to the NH_4^+-edge of the next layer (unbonded Cl atoms are represented by dark green spheres in Fig. 2, C to G).

The CMD-N-P_2 crystal synthesized had an elongated hexagonal shape (Fig. 2E, inset) that could be correlated with the hexagonal packing of the NH_4^+-edge atoms highlighted by the red hexagon (Fig. 2E). The NH_4^+-edge molecules were aligned along [1$\bar{1}$0], which was the fastest growth direction. In the same (001) layer of NH_4^+-edge, the hydrogen-bonded Cl atoms shifted along the [110] direction, as highlighted by the green hexagon, similar to the NH_4^+-edge positions of the second layer (Fig. E and F) with respect to the first layer and gave rise to AB stacking similar to the RP phase (Fig. 2G and fig. S2).

To investigate the stabilizing effect of intermolecular hydrogen bonding on the perovskite structure, we tried synthesizing the crystal with different halogen atoms (Cl, Br, and I) in the A-site cation, for example, *N*-bromomethyl-1,4-diazabicyclo[2.2.2]octonium (BMD^+) and *N*-iodomethyl-1,4-diazabicyclo[2.2.2]octonium (IMD^+). With NH_4^+ as the B-site cation, we tried growing BMD-N-P_2 and IMD-N-P_2, but only BMD-N-P_2 could be crystallized in the perovskite structure (figs. S6 and S7). With IMD^+, it crystallized in a monoclinic $P2_1/n$ symmetric group with a nonperovskite IMD-N_2-P_3 structure; an important clue was that this structure does not have N-H···I bond with NH_4^+ (fig. S8). This result suggested that the weaker N-H···I bond as compared with the N-H···Cl hydrogen bond destabilized the CL-v phase. Both CMD-N-P_2 and BMD-N-P_2 showed good thermal stability up to 200°C in air (fig. S9)

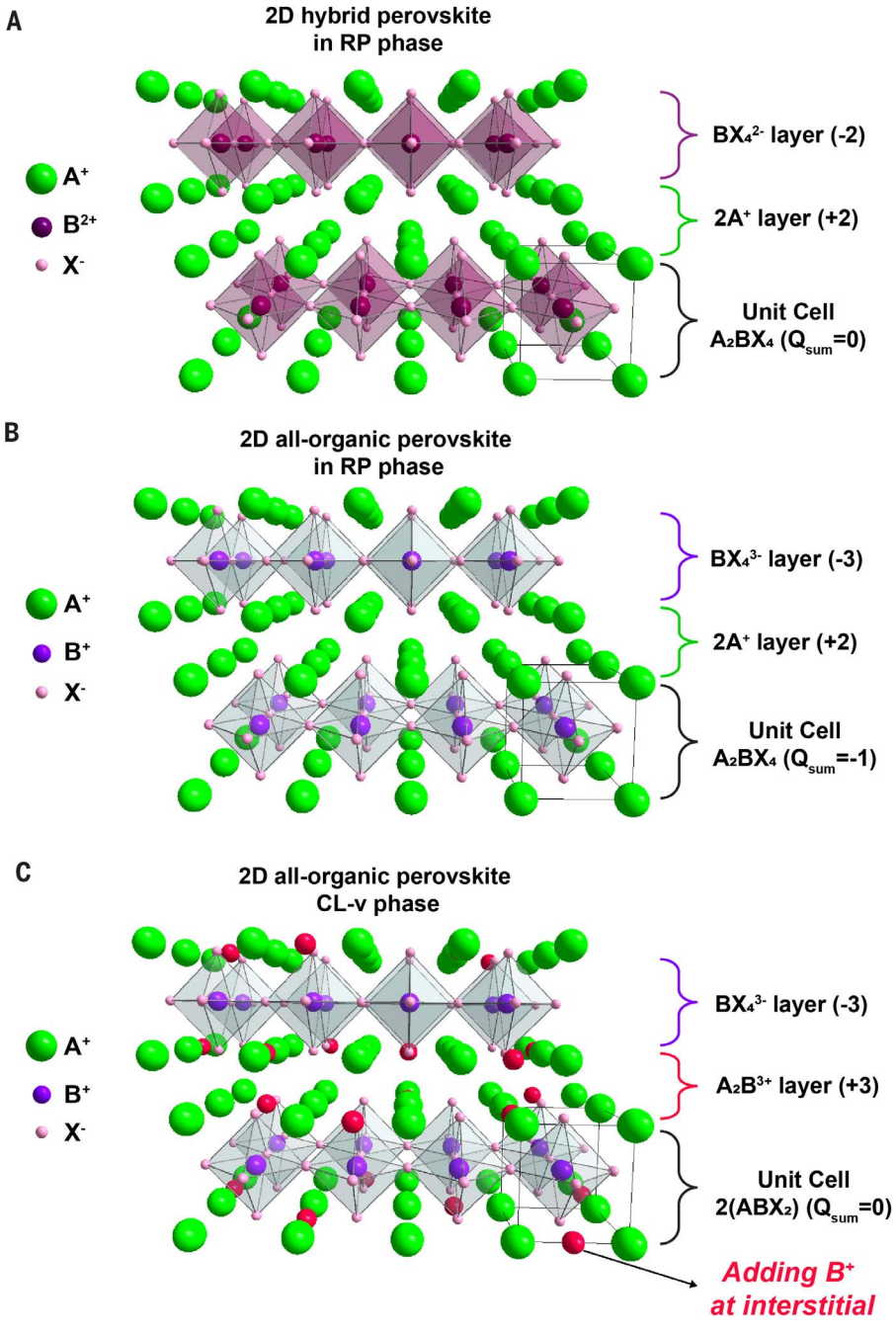

Fig. 1. Illustration of charge balance issues in 2D hybrid organic-inorganic RP phase and its all-organic analogs. (**A**) Charge compensated octahedral layer and spacer layer in a typical RP phase HOIP. (**B**) In the all-organic RP phase, charge imbalance occurs between the octahedral and spacer layers. (**C**) Addition of one interstitial B^+ cation in the spacer layer per unit cell balances the charge of the system.

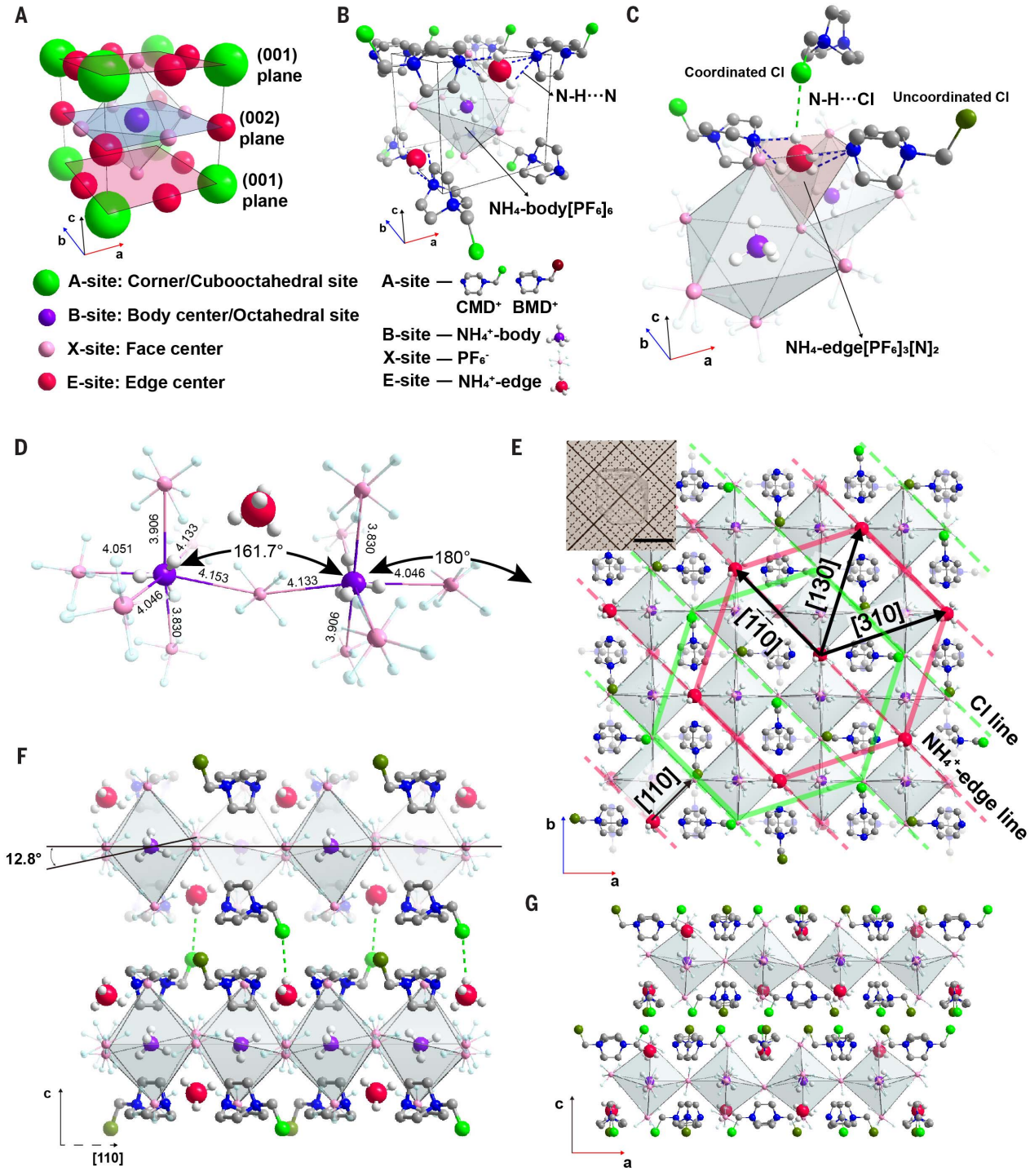

Fig. 2. Crystal structure description of CL-v. (**A**) A-, B-, and X-sites in the cubic cell, with the edge center (E-site) reserved for interstitial B^+ cation. (**B**) The pseudo-cubic unit cell of the CL-v phase is shown, with the NH_4-body$[PF_6]_6$ octahedron represented in light cyan. One NH_4^+-edge is located in the upper (001) plane and the other is in the bottom (001) plane. The E-site on (001) occupied with NH_4^+ has an occupancy of one-half because of sharing with one adjacent unit in the layered structure. CMD represents chloromethyl DABCO and BMD represents bromomethyl DABCO. Both the B-site and E-site consist of NH_4^+ ions, differentiated by the color of nitrogen for clarity. (**C**) The hydrogen bonding environment of the NH_4^+-edge, surrounded by three PF_6^- ions, two N-H···N bonds to create a $NH_4[PF_6]_3[N]_2$ translucent red pyramid. The Cl of CMD^+ in the adjacent layer forms an N-H···Cl bond with the NH_4-edge, resulting in the formation of an NH_4^+-edge$[PF_6]_3[N]_2[Cl]$ octahedron for stabilization of the NH_4^+-edge. Only half of CMD^+ forms N-H···Cl bonds, hence hydrogen bonded and non-bonded Cl are denoted in different colors. (**D**) The geometry of two NH_4-body$[PF_6]_6$ octahedrons with an NH_4^+-edge ion. Bond lengths in angstroms (Å). (**E**) View along the [001]direction. The unit vectors for NH_4^+-edge are $[1\bar{1}0]$, [130], and [310], with lengths of 11.6, 12.7, and 12.7 Å each. NH_4^+-edge and Cl atoms are arranged linearly in the $[1\bar{1}0]$direction and alternatingly in the $[\bar{1}10]$direction. Inset is 9 × 7 × 0.5 mm size hexagonal single crystal of CMD-N-P_2. (**F**) The view is along the NH_4^+-edge and Cl alignment direction $[\bar{1}10]$. The adjacent layers are held together by N-H···Cl bonds. (**G**) View along the [010] direction with two layers indicating AB stacking.

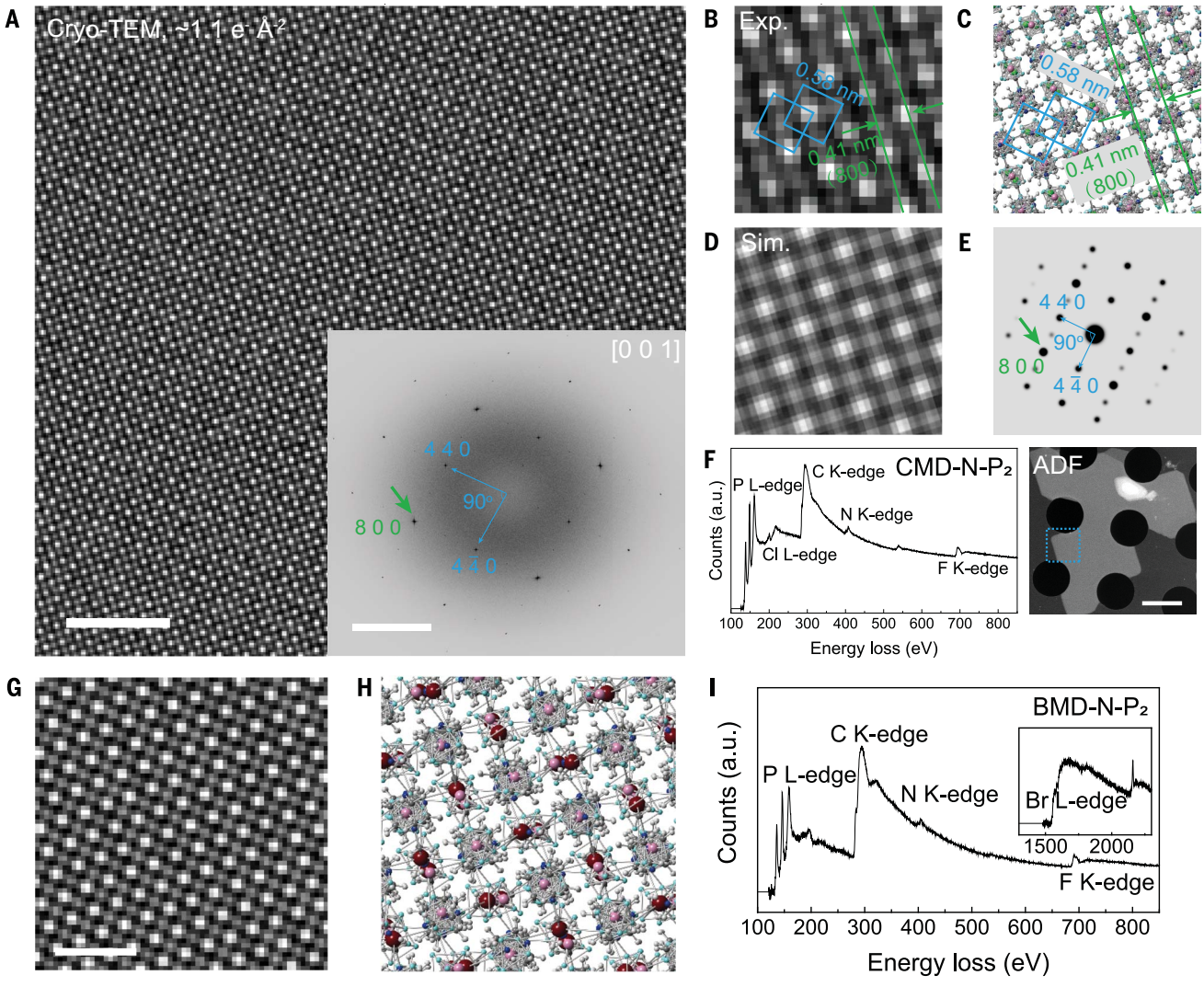

Fig. 3. Atomic structure and elemental characterization of the CL-v phases via cryo-TEM. (**A**) HRTEM image of CMD-N-P_2 taken along the [001] direction at ~77 K with an electron dose rate of ~0.68 e^- $Å^{-2}$ s^{-1} and a cumulative dose of ~1.1 e^- $Å^{-2}$. The inset displays the corresponding FFT pattern. (**B**) A magnified high-resolution image of CMD-N-P_2 lattice fringes from a selected area of image (A), and (**C**) the corresponding atomic model in the [001] axis. A bright spot in image (B) corresponds to a column of organic groups in image (C), demonstrating a perfectly matched periodic symmetrical structure, as emphasized by the blue squares. The green double lines indicate the interplanar spacing corresponding to the (800) lattice planes. Simulated experimental image (**D**) and reciprocal lattice (**E**) are based on the [001] oriented structural model in (C). (**F**) The EELS spectrum of CMD-N-P_2 exhibits clear onset features of P-L, Cl-L, C-K, N-K, and F-K edges, with a representative ADF image shown alongside. (**G**) HRTEM image, (**H**) atomic model along the [001] zone axis, and (**I**) EELS spectrum of BMD-N-P_2.

Cryo–transmission electron microscopy (TEM) analysis

Direct evidence of the perovskite-type lattice arrangement necessitates atomic TEM characterization of the various molecules in the lattice. We achieved near-atomic resolution imaging of the pure organic perovskite crystal structure under a cumulative electron dose of no more than 2 e^- $Å^{-2}$ in a cryogenic TEM (see supplementary materials for details and imaging conditions). In the case of CMD-N-P_2, Fig. 3A displays its large-area, high-resolution lattice-fringe image along the [001] zone axis. This image was acquired through successive short exposures at a dose rate of 0.68 e^- $Å^{-2}$ s^{-1} under a magnification of ×59000 (pixel size: 1.1 Å), with a total dose of ~1.1 e^- $Å^{-2}$. Columns of organic groups linked by covalent bonds were well-resolved in the enlarged HRTEM image, displaying an ideal cubic perovskite structure along the [001] projection, with a homogeneous alternation of bright and dim spots (Fig. 3B).

The square lattice, constructed by the smallest bright or dim spots, corresponded to the square repeating unit constructed by the columns of the A-site (CMD^+) plus B-site (NH_4^+) or columns of X-site (PF_6^-) plus NH_4^+-edge. As indicated by the blue boxes in Fig. 3B and 3C, the lattice spacing observed in the experiment completely aligned with that formed by CMD^+, and the atomic contrast was consistent with the result of the simulated HRTEM image at 100 nm defocus value (Fig. 3D and fig. S10). Additionally, the fast Fourier transform (FFT) pattern inserted in Fig. 3A closely matched the simulated reciprocal lattice (Fig. 3E), except for some extinction reflections reappearing in the FFT pattern because of dynamical scattering (thickness effect). The (800) reflection, marked by the green arrow, exhibits the highest diffraction intensity in both the FFT and the simulated reciprocal lattice, which corresponded to the lattice plane and is marked by green lines in Fig. 3, B and C, with an interplanar spacing of 0.41 nm. The chemical composition of the CMD-N-P_2 crystal, revealed by electron energy loss spectroscopy (EELS) in

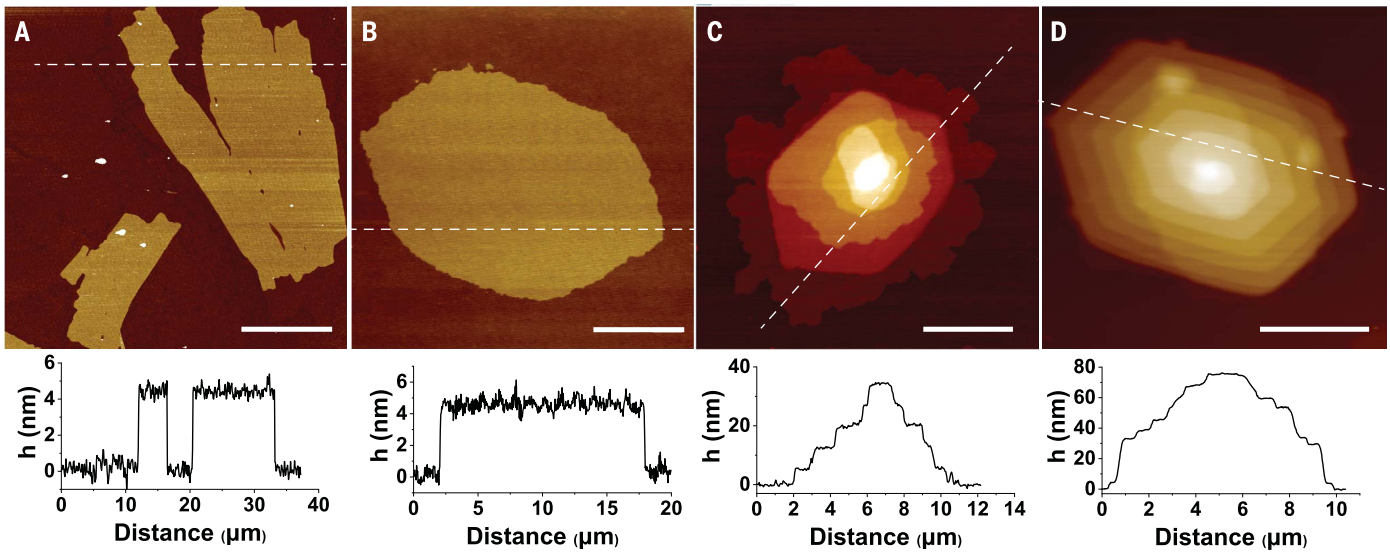

Fig. 4. Exfoliation and growth of CMD-N-P_2 ultrathin flakes. (**A**) AFM height image and line profile of 30 μm–sized CMD-N-P_2 exfoliated by sonication in dichloromethane. Scale bar is 10 μm. (**B**) AFM height image and line profile of CMD-N-P_2 grown on SiO_2 substrate with 0.1 weight percent (wt%) solution. Scale bar is 6 μm. (**C**) AFM height image and line profile of CMD-N-P_2 grown on SiO_2 substrate with 1 wt% solution, showing 6 layers. Scale bar is 3 μm. (**D**) AFM height image and line profile of a screw dislocation in the clockwise direction. Scale bar is 3 μm.

Fig. 3F, showed characteristic edges of P, Cl, C, N, and F, which matched its mechanically exfoliated bulk counterpart (figs. S11 and S12). We also tested another CL-v phase based on BMD-N-P_2, which shared similar crystal structure and lattice spacing with CMD-N-P_2, given that only the chloromethyl functional group in CMD^+ was replaced with bromomethyl. As depicted in Fig. 3G, the HRTEM image of BMD-N-P_2 crystals displayed a perovskite-type arrangement of the organic functional groups, similar to that shown in Fig. 3A with well-matched EELS (fig. S13).

Layered structure and exfoliation

The layered structure of CMD-N-P_2 was investigated with atomic force microscopy (AFM), which revealed a step height of 4.2 nm. Taking into account an overestimation of the thickness by ~1 nm by AFM measurement owing to tip-surface interactions, surface roughness, and trapped solvent (*31*, *32*), the closest thickness that matches this is the 2.56-nm–thick bilayer of the pseudo-cubic cell (fig. S2). Since we did not measure anything thinner than 2.56 nm, we assume that the alternating step is at least a bilayer. A distinctive attribute of van der Waals–stacked 2D materials is their ability to be exfoliated into molecularly thin flakes through solvent-based exfoliation of bulk crystals, and that the resulting flakes, assisted by sonication, disperse in solvents and exhibit the characteristic Tyndall effect of light scattering by a colloidal dispersion. The Tyndall effect of exfoliated CMD-N-P_2 and BMD-N-P_2 was weak in nonpolar solvents such as hexane and toluene. However, for aprotic polar solvents such as dichloromethane, the dispersion exhibited a strong Tyndall effect (figs. S14 and S15).

We inferred that the interlayer region of CMD-N-P_2 encompassed N-H···Cl bonds, and solvents containing chloro-functional groups could disrupt these interlayer hydrogen bonds by serving as H-bond acceptors. Thus, the exfoliated flakes were stabilized. Indeed, all chloro-functionalized solvents, including dichloromethane, 1,2-dichloroethane, 1-chlorohexane, chlorobenzene, and 1,3-dichlorobenzene, exhibited a strong Tyndall effect with CMD-N-P_2. Further confirmation of exfoliation was obtained through AFM characterization, which revealed that the flakes exfoliated by dichloromethane and 1,2-dichloroethane possessed a thickness as thin as ~4 nm, similar to the step height measured for layered crystal synthesized in this work (fig. S16). The largest flake size reached up to 30 μm when CMD-N-P_2 was sonicated in dichloromethane (Fig. 4A).

Exploiting the ability of solvents with chloro-functional groups to disrupt interlayer N-H···Cl bonds, we successfully demonstrated controlled growth of CMD-N-P_2 on a silica substrate. Gradual evaporation of a CMD-N-P_2 solution in the presence of 1,2-dichloroethane led to the precipitation of hexagonal-shaped flakes measuring 10 μm in width (Fig. 4B). We also obtained similar results for BMD-N-P_2 (fig. S17). Moreover, by adjusting the concentration of the CMD-N-P_2 solution, we can synthesize crystals as thin as ~4 nm (Fig. 4C). Thus, our findings highlight the potential to grow 2D layered organic crystals using a solution-based approach while achieving meticulous thickness control. The crystalline nature of the CMD-N-P_2 flakes grown using this method was evident from the presence of screw dislocations in some flakes, exhibiting both clockwise (Fig. 4D) and counterclockwise (fig. S18) dislocations with a step height of ~4 nm (*33*, *34*).

Applications of gate dielectric in 2D electronics

The ability of 2D all-organic perovskites to form molecularly thin films over large areas, combined with their insulating nature, makes them suitable as dielectric layers in 2D electronics. The optical band gaps of CMD-N-P_2 and BMD-N-P_2 were determined from the intercepts of the Tauc plots to be 5.56 eV and 4.69 eV, respectively (Fig. 5A). The wave functions were mostly localized in the molecules in these crystals, yielding a large band gap and small bandwidth <0.02 eV, as seen from the band structure calculated with density functional theory (DFT) (fig. S19). The DFT-calculated band gaps of 4.81 and 4.14 eV of CMD-N-P_2 and BMD-N-P_2 were underestimated but agreed with the experimental trends qualitatively and indicate that the Coulombic potential of atomic nuclei such as Cl and Br affects the gap (fig. S19) (*29*).

The dielectric constants of CMD-N-P_2 and BMD-N-P_2 were measured in the range of 1 kHz to 1 MHz, giving values of 4.86, and 5.53, respectively (Fig. 5B), which were higher than the dielectric constant of SiO_2 (3.9), but lower than HfO_2 (25). The breakdown fields of CMD-N-P_2 and BMD-N-P_2 are found to be 23 MV m^{-1} and 17 MV m^{-1}, respectively (fig. S21). These values are higher than those of hBN (12 MV m^{-1}), Alumina (13.4 MV m^{-1}) and

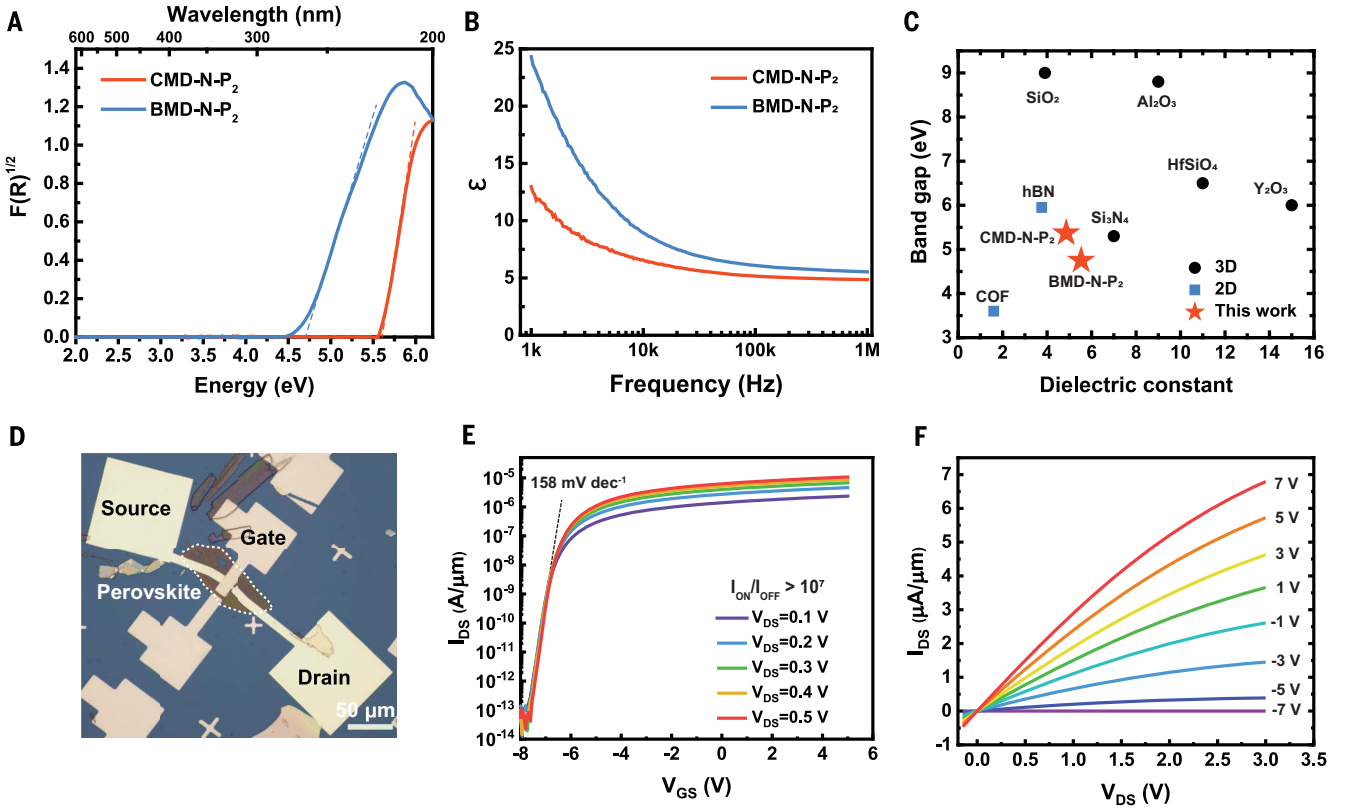

Fig. 5. Dielectric properties of CL-v family and FET device using CL-v phases as dielectric layer. (**A**) Tauc plot of the CL-v perovskites. (**B**) The dielectric constant of the CL-v perovskites displayed from 1 kHz to 1 MHz. (**C**) Dielectric constant and band gap values of the CL-v perovskites versus other dielectric materials. (**D**) Optical microscope image of FET using 100 nm CMD-N-P_2 as a dielectric layer. The transfer curve (**E**) and output curve (**F**) of FET with BMD-N-P_2 as a dielectric layer. Subthreshold swing is 158 mV per decade (dec^{-1}).

polystyrene (19.7 MV m^{-1}). Compared to 2D dielectric materials such as hexagonal boron nitride, CL-v phases have both a high dielectric constant and a large band gap, which makes them suitable for use as dielectric layers in 2D electronics (Fig. 5C). To demonstrate the effectiveness of CL-v phases as gate dielectric layers, we fabricated a field-effect transistor (FET) by transferring ≈100 nm-thick CMD-N-P_2 or BMD-N-P_2 as the top gate dielectric layer on MoS_2 as the channel material, and with Cr/Au metal as the source and drain electrodes. Figure 5D shows an optical image of a fabricated FET device. The measured transfer curve at different V_{ds} displays n-type behavior and the on-off ratio is $>10^7$ when the V_{ds} is 0.5 V, which is sufficient to comply with the standard of practical logic circuits of 10^4 (Fig. 5E) (*35*). The negligible hysteresis in the transfer curve suggested that a clean contact formed between the dielectric and channel material. Furthermore, a low subthreshold swing of 158 mV per decade was extracted from the transfer curve, which was lower than that of Al_2O_3 grown through atomic-layer deposition (*36*) The drain current–voltage (I_d–V_d) output curves exhibit linear characteristics at low bias. (Fig. 5F)

Conclusions

We designed and synthesized a new class of 2D organic perovskites known as the CL-v phase. Our synthetic approach is versatile and can be extended to various organic molecules as A-site cations, including diazabicycloalkane (*37*, *38*), azaadamantane (*39*), and other derivatives of heterocyclic compounds (*40*), as well as different B-site cations and X-site anions (fig. S23). CL-v phase can be exfoliated or grown as molecular thin crystalline organic layers with large aspect ratio by solution process, which can be potentially used as flexible dielectrics. Our findings enhance the understanding of structural design principles pertaining to all-organic perovskites. Based on this understanding, we posit that it is feasible to conceive and synthesize all-organic perovskite analogs of the Dion-Jacobsen and Aurivillius phases.

REFERENCES AND NOTES

1. W. Zheng *et al.*, *Adv. Mater.* **35**, e2205410 (2023).
2. L. T. Nguyen, R. J. Cava, *Chem. Rev.* **121**, 2935–2965 (2021).
3. S. Royer *et al.*, *Chem. Rev.* **114**, 10292–10368 (2014).
4. M. A. Peña, J. L. G. Fierro, *Chem. Rev.* **101**, 1981–2017 (2001).
5. L. N. Quan *et al.*, *Chem. Rev.* **119**, 7444–7477 (2019).
6. J. Y. Kim, J.-W. Lee, H. S. Jung, H. Shin, N.-G. Park, *Chem. Rev.* **120**, 7867–7918 (2020).
7. S. N. Ruddlesden, P. Popper, *Acta Crystallogr.* **10**, 538–539 (1957).
8. S. N. Ruddlesden, P. Popper, *Acta Crystallogr.* **11**, 54–55 (1958).
9. M. Dion, M. Ganne, M. Tournoux, *Mater. Res. Bull.* **16**, 1429–1435 (1981).
10. B. Aurivillius, *Ark. Kemi* **1**, 463–480 (1949).
11. B. Aurivillius, *Ark. Kemi* **2**, 519–527 (1950).
12. C. A. Bremner, M. Simpson, W. T. A. Harrison, *J. Am. Chem. Soc.* **124**, 10960–10961 (2002).
13. G.-Z. Liu, J. Zhang, L.-Y. Wang, *Synth. React. Inorg. Met.-Org. Nano-Met. Chem.* **41**, 1091–1094 (2011).
14. H.-Y. Ye *et al.*, *Science* **361**, 151–155 (2018).
15. S.-L. Chen *et al.*, *Sci. China Mater.* **61**, 1123–1128 (2018).
16. G.-M. Fan, C. Shi, L. Qiao, H.-J. Li, H.-Y. Ye, *J. Mater. Chem. C Mater. Opt. Electron. Devices* **6**, 8349–8352 (2018).
17. H. Morita *et al.*, *Angew. Chem. Int. Ed.* **58**, 9184–9187 (2019).
18. T. W. Kasel *et al.*, *Chem. Sci.* **10**, 8187–8194 (2019).
19. W.-X. Zhang, S.-L. Chen, Y. Shang, Z.-H. Yu, X.-M. Chen, *Energetic Materials Frontiers* **1**, 123–135 (2020).
20. Y. Shang *et al.*, *Cryst. Growth Des.* **20**, 1891–1897 (2020).
21. H. Morita, R. Tsunashima, S. Nishihara, T. Akutagawa, *CrystEngComm* **22**, 2279–2282 (2020).
22. J.-J. Wang, D. Fortino, B. Wang, X. Zhao, L.-Q. Chen, *Adv. Mater.* **32**, e1906224 (2020).
23. X. Song, G. Hodes, K. Zhao, S. Liu, *Adv. Energy Mater.* **11**, 2003331 (2021).
24. Y. Gao *et al.*, *ACS Appl. Mater. Interfaces* **13**, 19042–19047 (2021).
25. H. S. Choi *et al.*, *Nat. Commun.* **13**, 794 (2022).
26. H.-S. Wu *et al.*, *Adv. Sci* **9**, e2105974 (2022).
27. R. Taheri-Ledari *et al.*, *Energy Fuels* **36**, 10702–10720 (2022).
28. T. Handa *et al.*, *Science Advances* **8**, eabo1621 (2022).

29. Z. Li *et al*., *Adv. Mater.* **35**, e2300480 (2023).
30. L. Mao, C. C. Stoumpos, M. G. Kanatzidis, *J. Am. Chem. Soc.* **141**, 1171–1190 (2019).
31. C. J. Shearer, A. D. Slattery, A. J. Stapleton, J. G. Shapter, C. T. Gibson, *Nanotechnology* **27**, 125704 (2016).
32. X. Li *et al*., *Nat. Chem.* **12**, 1115–1122 (2020).
33. Y. Zhao, S. Jin, *Acc. Mater. Res.* **3**, 369–378 (2022).
34. Y. Zhao *et al*., *Science* **370**, 442–445 (2020).
35. M. Chhowalla, D. Jena, H. Zhang, *Nat. Rev. Mater.* **1**, 16052 (2016).
36. A. Sebastian, R. Pendurthi, T. H. Choudhury, J. M. Redwing, S. Das, *Nat. Commun.* **12**, 693 (2021).
37. S. F. Nelsen, J. M. Buschek, *J. Am. Chem. Soc.* **96**, 7930–7934 (1974).
38. S. F. Nelsen, P. J. Hintz, *J. Am. Chem. Soc.* **94**, 7114–7117 (1972).
39. A. I. Kuznetsov, V. A. Kosmakov, B. V. Unkovskii, *Chem. Heterocycl. Compd.* **21**, 697–700 (1985).
40. M. W. Giuliano, C.-Y. Lin, D. K. Romney, S. J. Miller, E. V. Anslyn, *Adv. Synth. Catal.* **357**, 2301–2309 (2015).

ACKNOWLEDGMENTS

Funding: This work was supported by project P0043087 Design and Synthesis of Hybrid Organic Inorganic Perovskites of Hong Kong Polytechnic University as well as funding from Hong Kong Jockey Club STEM lab of 2D Quantum Material (2023-0033). K.L. acknowledges the Croucher Foundation (Croucher Tak Wah Mak Innovation fund 2023) and projects 62322413 and 12104382 supported by National Natural Science Foundation of China and the Research Grants Council of the Hong Kong Special Administrative Region, China (projects PolyU25305222, PolyU15305221, and PolyU15304623) J.Y. acknowledges financial support from Hong Kong Polytechnic University (grant P0042930) and a grant from the Research Grants Council of Hong Kong (project PolyU 25300823).This project is partially supported by the National Natural Science Foundation of China (11974156), Guangdong Innovative and Entrepreneurial Research Team Program (grant 2019ZT08C044), Shenzhen Science and Technology Program (KQTD20190929173815000 and 20200925161102001), the Science, Technology and Innovation Commission of Shenzhen Municipality (ZDSYS20190902092905285). TEM/STEM characterization was performed at the cryo-EM Center and Pico Center from SUSTech Core Research Facilities that receives support from the Presidential Fund and Development and Reform Commission of Shenzhen Municipality.
Author contributions: H.S.C. and K.P.L conceived the idea and developed the project plan. H.S.C. designed, synthesized, grew bilayers, and characterized the CL-v crystals. K.P.L. supervised the research. J.L. and K.L. fabricated and characterized the FET device. G.W., F.L., and J.L. performed cryo-TEM measurements. W.P.D.W and I.H.P. conducted the single-crystal XRD structure analysis. J.Y. conducted DFT calculations of band gap. H.S.C. and K.P.L. wrote the manuscript with contributions from all authors. H.S.C., J.L., and G.W. contributed equally. **Competing interests:** The authors declare no competing interests. **Data and materials availability:** The data that support the plots within this article and other findings of this study are available from the corresponding author upon reasonable request.

SUPPLEMENTARY MATERIALS

science.org/doi/10.1126/science.adk8912
Materials and Methods
Figs. S1 to S23
Tables S1 to S3
References (*41*–*43*)

Submitted 19 October 2023; accepted 22 February 2024
10.1126/science.adk8912